S S Denk et al.

Analysis of electron cyclotron emission with extended electron cyclotron forward modeling

Analysis of electron cyclotron emission with extended electron cyclotron forward model for routine application

S. S. Denk,[1,2] R. Fischer,[1] H. M. Smith,[3] P. Helander,[3] O. Maj,[1] E. Poli,[1] J. Stober,[1] U. Stroth,[1,2] W. Suttrop,[1] E. Westerhof,[4] M. Willensdorfer,[1] and the ASDEX Upgrade Team[1]

[1) *Max Planck Institute for Plasma Physics, Boltzmannstr. 2, 85748 Garching, Germany*

[2) *Physik-Department E28, Technische Universität München, 85748 Garching, Germany*

[3) *Max Planck Institute for Plasma Physics, D-17491 Greifswald, Germany*

[4) *DIFFER - Dutch Institute for Fundamental Energy Research, De Zaale 20, 5612 AJ Eindhoven, the Netherland*

At the ASDEX Upgrade tokamak the electron temperature (T_e)-profile is estimated from electron cyclotron emission (ECE) using radiation transport forward modeling within the integrated data analysis scheme. For the interpretation of Electron Cyclotron Emission (ECE) measurements in high $T_e > 5\,\mathrm{keV}$ plasmas, it was necessary to upgrade the forward model with a fully relativistic absorption coefficient including the relativistic Maxwell-Jüttner distribution.

This model intrinsically enables the interpretation of ECE measurements affected by the so-called "pseudo-radial displacement" or by harmonic overlap. A numerically efficient implementation allows for the analysis of everyday ECE measurements at ASDEX Upgrade. Various ASDEX Upgrade plasma scenarios are discussed highlighting the benefits of the present radiation transport forward modeling for routine analysis.

I. INTRODUCTION

ECE is one of the primary diagnostics for estimating the electron temperature (T_e) profile in magnetically confined fusion research due to its high temporal and spatial resolution[1].

A calibrated ECE diagnostic measures radiation temperature (T_{rad}) for a set of measurement frequencies ω. Often it is possible to infer T_e from T_{rad} via the Rayleigh-Jeans law[2]. The position of the T_e measurement is determined by ω and is usually mapped to the cold resonance position, where ω is equal to the fundamental or an harmonic of the cyclotron frequency[2]. Most frequently the radiometer is optimized such that the second harmonic eXtraordinary mode (X-mode) is the main contributor to the observed T_{rad}.

However, this ubiquitous approach to interpret the ECE measurements becomes inadequate if (I) emission from plasma layers other than the cold resonance position contributes either due to relativistically down-shifted emission or due to Doppler-shifted emission in case of oblique lines of sight (LOS). The same applies if (II) the optical depth of the measurement is low, or if (III) harmonic overlap occurs. For low absorption near the cold resonance, emission from additional plasma layers can pass through the cold resonance layer resulting in a shine-through of down-shifted emission. This occurs typically near the plasma edge and in the near scrape-off layer (SOL) in high-confinement mode (H-mode) plasmas, where emission from the pedestal top and the gradient region is observed in channels with cold-resonance positions in the near SOL region. The shine-through radiation causes the T_{rad} profile to show a peak structure in the near SOL, which is called a shine-through peak[3,4]. Low optical depth at elevated temperatures ($T_e > 7\,\mathrm{keV}$) can result in shine-through of heavily down-shifted emission from relativistic electrons at the plasma core. Furthermore, even in the case of large optical depth, a locally small absorption in the plasma core can result in a so called "Pseudo radial displacement" (PRD)[5] of the ECE measurements near the plasma core.

To overcome the density cut-off of the second harmonic extraordinary (X-) mode, measurements of the third harmonic X-mode spectrum can be used. However, this poses the problem of harmonic overlap, i.e. in addition to the third harmonic resonance on the low-field side (LFS), there can be also (at low torus aspect ratio) a resonance with the second harmonic on the high-field side (HFS). Finally, for oblique LOSs the Doppler effect can displace the origin of the observed radiation from the cold resonance position[6].

Radiation transport modeling in the framework of Integrated Data Analysis (IDA)[7] allows one to resolve all of these issues. A reliable reconstruction of T_e profiles in H-mode from ECE measurements considering shine-through emission and Doppler broadening is obtained for second harmonic X-mode spectra with relatively large electron density (n_e) and moderate T_e applying a previous electron cyclotron emission forward model (ECFM)[4]. In the present work the radiation transport model presented in ref.[8] is applied, which extends the utility of the radiation transport method to high T_e plasma scenarios and ECE measurements affected by third harmonic emission.

This paper is structured as follows. In section II the ASDEX Upgrade profile radiometer is presented. In section III the radiation transport models described in ref.[8] and ref.[4] are compared. Section IV shows new applications of the advanced forward model. Conclusions are drawn in section V.


II. THE ELECTRON CYCLOTRON EMISSION DIAGNOSTIC AT ASDEX UPGRADE

At ASDEX Upgrade a 60-channel heterodyne radiometer is used for ECE measurements. The LOS of the ECE system are close to the mid-plane. The antennae are located at the LFS[4,9]. Figure 1 illustrates the optics of the ECE diagnostic. A quasi-optical system of three lenses focuses the radiation emitted by the plasma into a rectangularly arranged bundle of wave guides with three rows and four columns. These wave guides are illustrated by the small rectangles on the left side of figure 1. For clarity only the optical paths of two wave guides are shown in each of the figures. The axis of the quasi-optical system, which is shared with an ECE Imaging diagnostic[6], is aligned with the center of the wave guide bundle. The wave guides are all parallel to each other and since there are four columns, none of the LOS is perfectly radial. For the two inner wave guides the toroidal viewing angle (i.e. the deviation from a perfectly radial view) is $\phi_{tor} = \pm 0.7°$ and for the two outer wave guides $\phi_{tor} = \pm 2.2°$.

The ASDEX Upgrade profile radiometer is designed to observe the emission of the second harmonic X-mode. Please note that in this paper the designation of X and O mode refers to propagation perpendicular to the magnetic field. The polarization filter is a wire grid aligned with the toroidal direction of the torus. Due to a small but non-zero pitch angle of
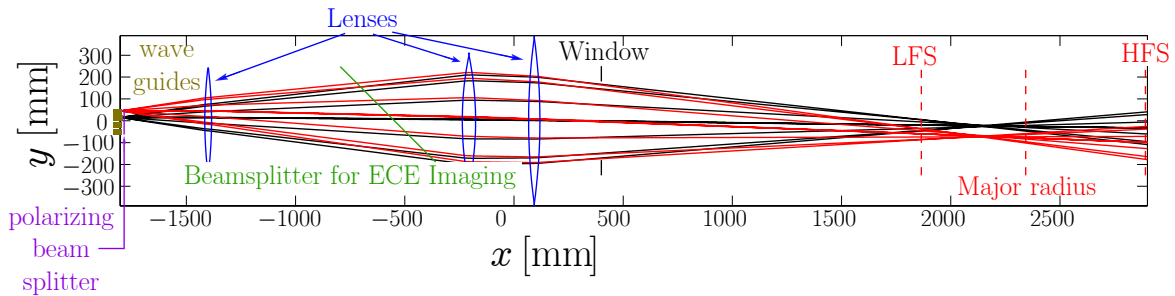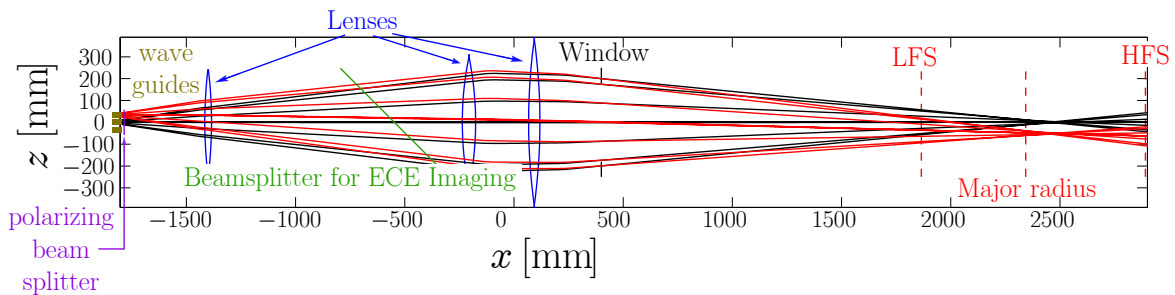
FIG. 1. The optics of the ASDEX Upgrade profile radiometer viewed from (a) the top and (b) the side.

the magnetic field and the deviation from a perfectly radial view a contribution of O-mode radiation is expected. The radiation transport model presented in ref.[8] was extended to include the polarization filter allowing the O-mode contribution to the measurements to be evaluated. The calculated T_{rad} spectra considering the superposition of the O- and the X-mode tend to be at most 5 % smaller than the pure X mode spectra, if wall reflections are considered. Accounting for the O-mode in the analysis of the ECE measurements doubles the computational cost. Since the contribution of the O-mode emission is expected to be small it is neglected in the routine evaluation of the measurements. Accordingly all synthetic spectra shown throughout this paper are pure X-mode spectra and the impact of O-mode contributions to the measured ECE spectra is not discussed in this paper.

The radiometer covers a frequency range from 84.3 to 143.6 GHz. For ASDEX Upgrades typical magnetic field strength ($|B_t| \approx 2.5\,T$) the resonance positions are chosen such that they cover the region from a few centimeters on the HFS close to the magnetic axis and the entire LFS including the SOL. 36 of the 60 channels feature a bandwidth of 300 MHz

4

in the intermediate frequency, which corresponds to a spatial resolution (disregarding frequency broadening effects) of $\approx 0.5\,\mathrm{cm}$ at the plasma edge. The channels are distributed non-equidistantly with a typical spacing of $400\,\mathrm{MHz}$. The other 24 channels have a wider bandwidth of $600\,\mathrm{MHz}$ and a frequency spacing of approximately $1\,\mathrm{GHz}$. This translates into a spatial resolution of $\approx 1.2\,\mathrm{cm}$ at the plasma core. The profile radiometer is absolutely calibrated with the hot-cold source technique[10]. The estimated systematic error of the calibration is $7\,\%$. The ECE measurements are sampled with a frequency of $1\,\mathrm{MHz}$. The measurements shown in this work are averaged over $1\,\mathrm{ms}$. The error bars indicate the sum of the systematic uncertainty and one standard deviation from the temporal average.

III. THE IMPROVED RADIATION TRANSPORT MODEL

The previous ECFM[4] is compared with the present, improved radiation transport model[8] by using plasma scenarios with significant shine-through from the core to the edge due to the heavily down-shifted emission of relativistic electrons. However, a straightforward comparison of the ECFM presented in ref.[4] with the improved radiation transport model proposed in ref.[8] is not possible. For the selected scenarios the model of ref.[4] faces issues with numerical stability and validity limitations of the employed physical model. It is emphasized that these problems arise only for the type of scenarios addressed in this paper, whereas the results presented in[4] are not affected. Three improvements are made to the previous ECFM[4] for the benchmark against the improved radiation transport model of ref.[8]:

1. The cut-off density of the second harmonic X-mode was approximated as $n_\mathrm{co}^{2X} = \frac{\epsilon_0 m_{\mathrm{e},0}}{2e^2} 2\omega_{\mathrm{c},0}{}^4$, with ϵ_0 the vacuum permittivity, $\omega_{\mathrm{c},0} = \frac{eB}{m_{\mathrm{e},0}}$ cyclotron frequency, B the total magnetic field strength, $m_{\mathrm{e},0}$ is the rest mass of the electron and e the elementary charge. This approximation makes use of the assumption that the measurement frequency ω equals twice the cyclotron frequency. While this approximation holds for the cold resonance position of the second harmonic, it is invalid for strongly down-shifted emission for which $\omega < 2\omega_{\mathrm{c},0}$. Instead, the cold plasma refractive index is used to identify the regions of the LOS where the microwaves are evanescent. This is more consistent with the cold plasma raytracing performed in the improved radiation transport model.

5

2. The analytical solution of the emissivity integral is observed to be numerically unstable for strongly down-shifted emission $\omega < 2\omega_{c,0}$. The stability issues are caused by the numerical implementation of the Dawson Integral which is required by the analytical solution. Replacing the analytical solution of the integral with a numerical integration scheme avoids this issue.

3. The forward Euler solver for the radiation transport differential equation is replaced with a 4th order Runge-Kutta integrator, which improves numerical stability.

For the following comparison of the two models the modified version of the ECFM[4] is denoted as model A. The model presented in ref.[8] will be referred to as model B.

A. Similarities between the two models

Both models A and B first calculate the LOS and then solve the radiation transport equation along the LOS in a second step. Both models assume a thermal plasma and apply Kirchhoff's law relating the emissivity and the absorption coefficient. For the comparison only the second harmonic X-mode emission is considered, because unlike model B, model A was not designed for any other harmonic or polarization. Furthermore, an infinite reflection model is used in both models to include the effect of wall reflections[4,8]. The wall reflection coefficient is chosen to be $R_{\mathrm{wall}} = 0.9$ for all calculated T_{rad} profiles in this paper. This value has been proven to be reasonable for most ASDEX Upgrade plasmas that exhibit a shine-through peak.

B. Improvements

Compared to model A, Model B has four major improvements:

1. Instead of a non-relativistic approximation of the single-electron emissivity[2,4], a fully relativistic "polarization factor"[8,11] is used.

2. Instead of straight LOS[4], cold-plasma geometrical-optics raytracing is applied[8].

3. Instead of a tenuous plasma dispersion relation for the emissivity/absorption coefficient[2,4,8], the cold-plasma dispersion relation is used[11].

4. Instead of a non-relativistic Maxwellian[4], a fully relativistic Maxwell-Jüttner distribution for the emissivity/absorption coefficient is employed[8,11].

Another minor difference is that in model A the emissivity is calculated explicitly and the absorption coefficient is derived using Kirchhoff's law, while in model B the absorption coefficient is calculated explicitly and the emissivity is derived.

C.   Significance of improvements

To assess the significance of the various improvements implemented in model B, a hybrid model A' is introduced containing all improvements (1 to 3) except for the relativistic distribution function (4).

(a)   (b)   (c)
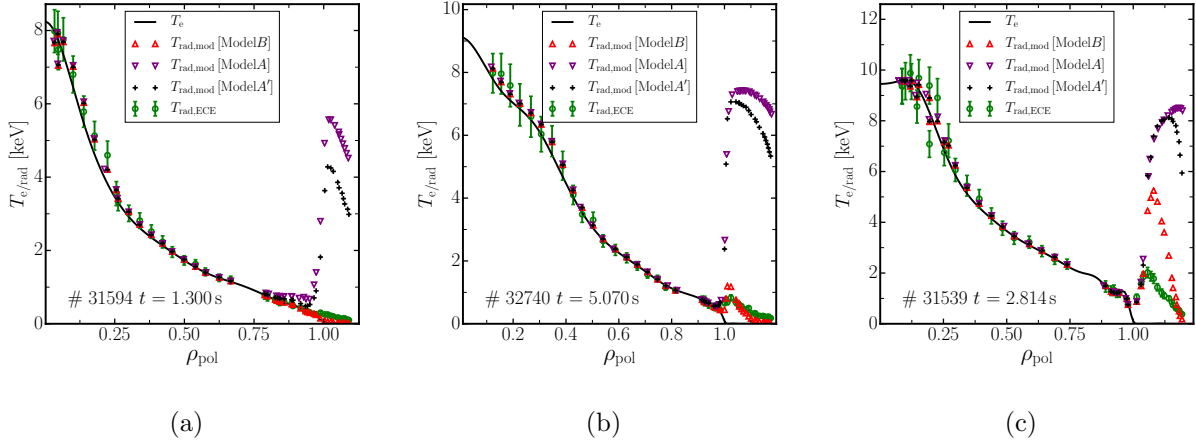
FIG. 2.   Estimated T_e profiles applying radiation transport modeling in the IDA scheme shown as a function of the normalized minor radius. Additionally, the measured $T_{rad,ECE}$ and modeled $T_{rad,mod}$ according to model A, A' and B are shown mapped to the cold resonance position of the second harmonic X-mode.

Figure 2 compares the radiation temperature T_{rad} evaluated with models A, A' and B ($T_{rad,mod}$) with the measured values $T_{rad,ECE}$ for three different scenarios. All three scenarios have strong central electron cyclotron resonance heating (ECRH), a correspondingly large T_e in the plasma core, and an on-axis magnetic field strength of about $B_t = -2.5\,\text{T}$. The main distinction is given by different on-axis electron densities n_e: (a) # 31594 at $t = 1.30\,\text{s}$ has a very low plasma core density of $n_e = 1.8 \times 10^{19}\,\text{m}^{-3}$; (b) # 32740 at $t = 5.06\,\text{s}$ is in

mainly helium with a plasma core density of $n_e = 3.0 \times 10^{19}\,\mathrm{m^{-3}}$; (c) # 31539 at $t = 3.29\,\mathrm{s}$ has a comparatively large plasma core density of $n_e = 4.7 \times 10^{19}\,\mathrm{m^{-3}}$.

The T_e-profile as a function of the square root of normalized poloidal flux ρ_{pol} is reconstructed using forward model B. The T_e- and n_e-profiles are estimated within the IDA framework combining measurements from ECE, interferometry[12] and lithium beam spectroscopy[13] for #31594 and #32097. Thomson Scattering (TS)[14] measurements of n_e replace the lithium beam spectroscopy measurement for #32740, because overlapping lithium and helium lines reduce the reliability of lithium beam spectroscopy in helium plasmas. The ECE measurements are mapped to cold resonance positions. Only ECE measurements within the confined region ($\rho_{pol} < 1$) were considered for estimating the T_e profile. Therefore, the comparison of the measured and forward modeled T_{rad} in the SOL ($\rho_{pol} \geq 1$) allows one to validate the various models.

For channels with cold resonance positions in the SOL, model B provides the best agreement between the measured and modeled T_{rad} even though these channels are not considered in the fit. Model A shows the worst agreement. Model A' including three out of the four improvements performs only little better compared to A. Although model B describes the relatively small measured ECE intensities reasonably well, there are residual discrepancies, especially in # 31539 (c.f. figure 2(c)). The residual discrepancy is discussed in section III E and section III F.

D.   Relativistic vs. non-relativistic distribution function

For the scenarios studied in ref.[4] with relatively large n_e ($> 5 \times 10^{19}\,\mathrm{m^{-3}}$) and moderate T_e ($< 5\,\mathrm{keV}$) the measurements and forward modeled T_{rad} were consistent. This was confirmed with model B. The different performance of models A, A' and B for the present plasma scenarios mainly results from the different energy distribution functions used and the shine-through of down-shifted emission from relativistic electrons in the plasma core. The origin of the radiation observed in the low-frequency channels is given by the birthplace distribution of observed intensity (BPD)[8,15]. The BPD of ECE measurements corresponds to the power deposition profile for ECRH. Figure 3 compares the BPDs from models A and B for the three corresponding test cases with different n_e in the plasma core. Negative (positive) values of ρ_{pol} correspond to positions on the HFS (LFS), respectively. An ECE channel with

cold resonance position at $\rho_{\mathrm{pol}} \approx 1.04$ (dashed line) was chosen.
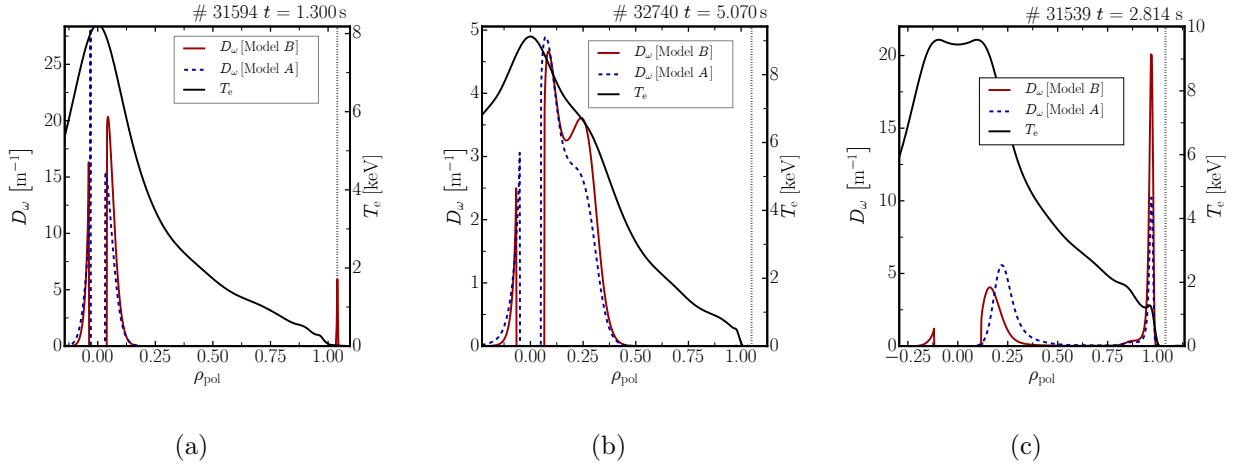

(a)   (b)   (c)

FIG. 3.   BPD for a cold resonance position of $\rho_{\mathrm{pol}} \approx 1.04$ calculated by model A and model B for the three plasma scenarios with different densities.

In all three cases a significant amount of the observed radiation originates from the plasma core, which was not observed for the scenarios discussed in ref.[4]. The gap in the BPD close to the plasma center arises from the LOS not going exactly through the plasma center.

The contribution of the plasma core relative to that of the plasma edge reduces with increasing density as expected due to the increasing optical depth. The large SOL peaks in T_{rad} predicted by models A and A' result from an overestimation of the strongly down-shifted radiation from electrons in the plasma core. The Maxwell distribution does not account for the relativistic mass increase resulting in an over-population of the relativistic speeds. With an on-axis magnetic field strength of $|B_{\mathrm{t}}| = 2.5\,\mathrm{T}$ the second harmonic of the cyclotron frequency is $2f_{\mathrm{c}} = 140\,\mathrm{GHz}$ in the plasma core. In contrast, the measurement frequency f_{ECE} of the channels for which the cold resonance positions lie in the SOL is only about $105\,\mathrm{GHz}$. If the down-shift is attributed to the relativistic mass increase only (i.e. if the Doppler shift is neglected), a Lorentz factor $\gamma = 1.4$ is required. This corresponds to an electron velocity $\beta = v/c_0 = 0.7$ and a kinetic energy of about $200\,\mathrm{keV}$. Figure 4 compares the Maxwellian with the Maxwell-Jüttner distribution for $T_{\mathrm{e}} = 8\,\mathrm{keV}$. For $\beta > 0.3$ the Maxwellian is significantly larger than its relativistic counterpart. The vertical lines in fig. 4 indicate the velocity contributing most to the down-shifted emission observed in the plasma edge ECE channels for the three scenarios. The variability of β from 0.55 to 0.60 is due to different Doppler shifts and BPDs. For the scenario with the smallest (largest) n_{e} shows the
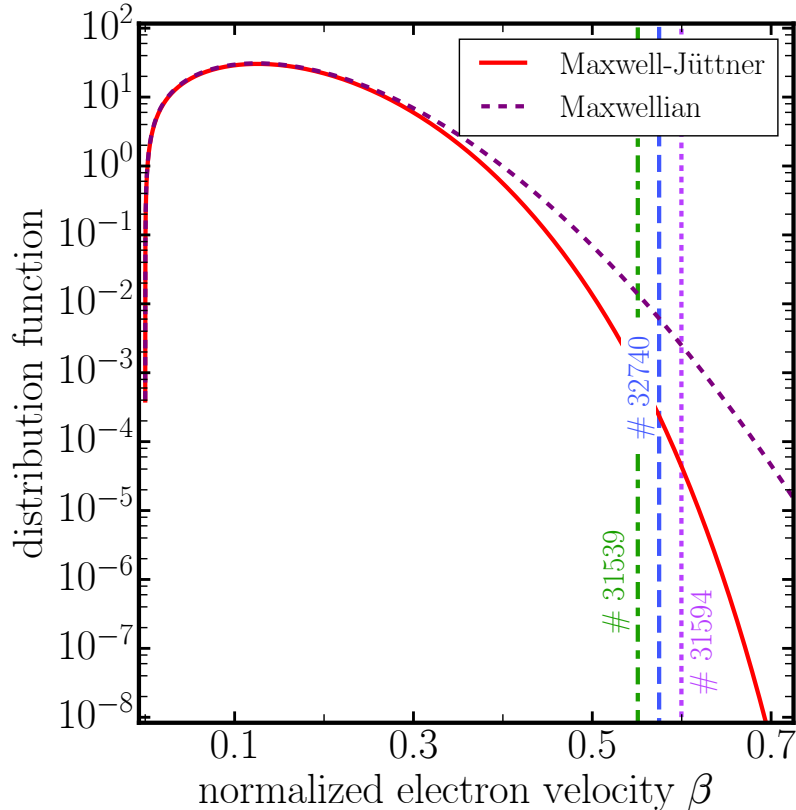
region with largest (smallest) frequency down-shift.

FIG. 4.   Maxwellian and Maxwell-Jüttner distribution for $T_{\mathrm{e}} = 8\,\mathrm{keV}$. The regions with significant down-shifted emission for the SOL channels shown in fig. 3

E.   The Abraham–Lorentz force

Model B describes small T_{rad}-values in the SOL region reasonably well for plasmas with either low T_{e} or low n_{e}, e.g., for the discharges #31594 and #32740. But it overestimates T_{rad} for plasmas with large core T_{e} and $n_{\mathrm{e}} > 4.0 \times 10^{19}\,\mathrm{m}^{-3}$, e.g., for #31539.

A candidate for an overestimation of T_{rad} is given by disregarding the Abraham–Lorentz force. This radiation reaction force might result in a depletion of the high-energy tail of a thermal distribution. Accordingly a reduction of the heavily down-shifted emission from relativistic electrons can arise. This would affect the measurements significantly because the emissivity and absorption coefficient scale strongly non-linearly with the velocity perpendicular to the magnetic field ($\propto \beta_{\perp}^4$). This effect would only be observable for cases with

significant intensity in the ECE channels originating from down-shifted core emission.

For estimating the effect of the Abraham–Lorentz force on ECE measurements the radiation drag has to be balanced with thermalizing collisions. For small velocities the radiation reaction force is expected to be negligible as the collision frequency is large. For relativistic velocities the radiation reaction force is expected to alter the thermal distribution due to a relatively small collision balancing term. To estimate the significance of the radiation reaction force on ECE measurements the linear solution for the steady-state electron distribution function resulting from the Abraham Lorentz force[16,17] and relativistic collisions[18] was calculated analytically assuming a homogeneous plasma and a dimensionless momentum $u = \gamma \cdot \beta = \frac{\beta}{\sqrt{1-\beta^2}} \approx 1$. The details on the calculation can be found in appendix A. The resulting steady state distribution

$$f = f_{\mathrm{MJ}}(u) \sum_{n=0}^{\infty} g_n(u) L_n(\zeta) \tag{1}$$

taking into account the radiation reaction force is expressed as a sum of Legendre Polynomials L_n with the pitch angle $\zeta = \left(\frac{u_\parallel}{u}\right)$ as argument. The pitch angle is given by the fraction of $u_\parallel$ the dimensionless momentum parallel to the magnetic field over the dimensionless, total momentum u. The coefficients of the Legendre Polynomials g_n are given by:

$$g_0 = -\alpha \left(\arctan(u) - u + \frac{u^3}{3} \right) \tag{2}$$

$$g_2 = \alpha \left(\frac{\gamma+1}{u} \right)^{3(Z+1)} \int_0^u \frac{u'^4}{\gamma'^2} \left(\frac{u'}{\gamma'+1} \right)^{3(Z+1)} \mathrm{d}u' \tag{3}$$

It can be shown that all other coefficients (g_1, $g_{n>2}$) are zero. The following variables were introduced in equations (2) and (3):

$$\gamma = \sqrt{1+u^2}, \qquad \alpha \equiv \frac{2\mu\tau}{3\tau_{\mathrm{r}}}, \qquad \mu = \frac{m_{\mathrm{e},0}c_0^2}{k_{\mathrm{b}}T_{\mathrm{e}}}, \qquad \tau = \frac{4\pi\epsilon_0^2 m_{\mathrm{e},0}^2 c_0^2}{n_{\mathrm{e}} e^4 \ln\Lambda}, \qquad \tau_{\mathrm{r}} = \frac{6\pi\epsilon_0 m_{\mathrm{e},0}^3 c_0^3}{e^4 B^2}$$

Where c_0 is the vacuum speed of light, Z the effective charge and $\ln\Lambda$ the Coulomb Logarithm. For the calculations the mean value of B on the flux surface and $Z = 1.5$ is considered.

This analytical solution was compared with a numerical solution obtained with the Fokker-Planck code RELAX[19], which was extended to include the Abraham Lorentz force. The deviation of the two non-thermal distributions from the thermal distribution was computed and normalized by the thermal distributions. The normalized deviations are shown

in figure 5(a) as functions of the dimensionless momentum perpendicular to the magnetic field $u_\perp$ for $u_\parallel = 0$ and $\rho_{\mathrm{pol}} = 0.2$. Both distributions show a depletion of high-energetic electrons of the order of 5 to 20 % in the relevant range of $u_\perp$ =0.6 to 0.8.

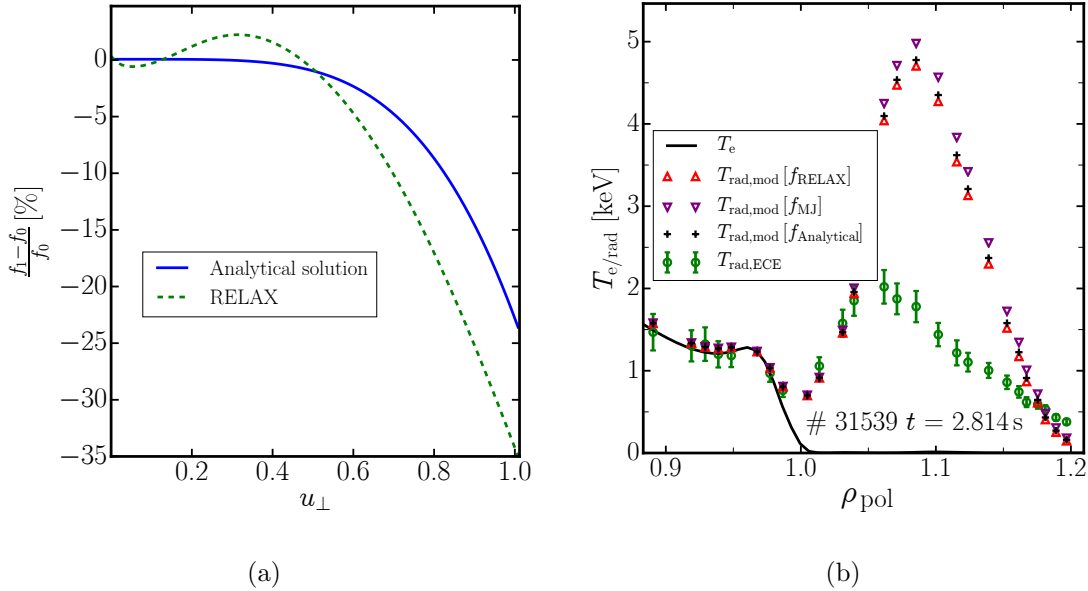(a)   (b)

FIG. 5.   a) The normalized deviations from a thermal distribution are shown for the analytical solution and the distribution function calculated by RELAX. b) Comparison of the forward modeled T_{rad} considering the analytically computed distribution, the distribution function from RELAX and a thermal distribution.

To calculate T_{rad} in the case of non-thermal distributions the radiation transport model presented in[8] was extended to include the absorption coefficient presented in ref.[11], which is valid for arbitrary distributions. In figure 5(b) the T_{rad} derived from the analytical distribution function and the distribution function from RELAX are compared to the thermal T_{rad} profile for the ECE channels with resonance positions in the SOL. The reduction of T_{rad} compared to the T_{rad} evaluated with a thermal distribution function is only in the order of a few %. This clearly shows that the effect of the Abraham Lorentz force is too small to be responsible for the overestimation of T_{rad}. The observed discrepancy between the modeled and the measured T_{rad} must therefore have a different reason.

F.   Wall reflections

Another candidate for the overestimation of T_{rad} is given by the simplified model of infinite wall reflections. The model of infinite reflections can become inaccurate if the optical depth is very small[20]. In this case a large number of direct reflections have to be added to obtain effectively an optically thick measurement. In #31539 the optical depth at the measurement frequencies where the discrepancies between model and experiment occur is below $\tau_\omega < 0.2$. In the idealized case of a perfectly reflecting wall (i.e. a wall reflection coefficient of 1) > 15 direct reflections are needed to provide a total optical depth $\tau_\omega > 3$. At very low optical depth wall reflections can cause the entire plasma to contribute to an ECE measurement[21]. For these cases ref.[20] suggests an entirely different wall reflection model. It is assumed that the radiation from the plasma is in thermal equilibrium with the wall. The wall then provides an initial radiation temperature to the radiation transport equation. For ECE measurements in the mid-plane this model predicts a significantly smaller contribution to T_{rad} than the infinite reflection model employed in model B. Therefore, the residual discrepancy comparing measured and modeled T_{rad} is interpreted as a consequence of the simplified infinite wall reflection model. Unfortunately, both, the approach given by ref.[20] and an even more sophisticated model for wall reflections at very low optical depth, that considers radiation transport, is challenging and the computational cost is too high to justify the use in routine data analysis. Summarizing, model B is not reliable in predicting T_{rad} accurately for measurements with an optical depth of about $\tau_\omega < 0.5$.

IV.   APPLICATIONS OF ELECTRON CYCLOTRON RADIATION TRANSPORT MODELING

In standard plasma scenarios with relatively large n_{e} and moderate T_{e}, radiation transport modeling describes the shine-through peak at the plasma edge as relativistic down-shift of emission from the pedestal top through the steep H-mode pedestal gradient without the need for non-thermal electrons[4]. For routine evaluation of ECE measurements in a broad operational space, radiation transport modeling has to reliably describe the effects observed in all plasma scenarios. This includes the two cases: "Pseudo-radial displacement" (PRD) at the plasma core and measurements affected by harmonic overlap.

A. "Pseudo radial displacement" at the plasma core

At high T_e and low n_e ECE measurements are known to show a PRD[5], which was observed, e.g. , at ASDEX Upgrade[22,23], JET[24], DIII-D[25] and TORE-SUPRA[26]. The PRD is observed for large T_e-gradients in the plasma core. It results from reduced absorption close to the cold resonance position and a corresponding shining of down-shifted emission through the cold resonance. PRD is already intrinsically included in the radiation transport model of ref.[4]. However, PRD is observed at ASDEX Upgrade only in high T_e discharges where the usage of a non-relativistic Maxwellian is inappropriate for the interpretation of the plasma edge ECE measurements. The improved model allows the consistent description of ECE measurements in scenarios with PRD.

The PRD can best be seen if the ECE channels are mapped to magnetic coordinates. A loop structure in T_{rad} indicates a PRD as temperature is expected to be constant on flux surfaces. A similar loop structure might also occur (and is observed) when the flux surfaces of the magnetic equilibrium are inaccurately estimated. An erroneous radial displacement of the magnetic axis and inner flux surfaces can also be seen in a loop structure. The two sources of the loop in $T_{rad,ECE}(\rho_{pol})$ can be distinguished by radiation transport modeling. The loop structure by PRD can be described by radiation transport modeling whereas a residual loop not modeled properly with radiation transport indicates an erroneous equilibrium. This residual loop structure provides valuable information to improve the equilibrium employing iso-flux constraints to the equilibrium reconstruction[27].

Figure 6 shows ECE measurements from discharge # 30907 at $t = 0.73\,$s with a large T_e-gradient and a relatively small $n_e \approx 1.2 \times 10^{19}\,\mathrm{m}^{-3}$ in the plasma core. Negative (positive) values of ρ_{pol} correspond to cold resonance positions on the HFS (LFS), respectively. T_{rad} on the HFS (LFS) is smaller (larger) than T_e at the cold resonance position, respectively. This displacement is due to the low absorption at the cold resonance position and the shine of down-shifted radiation through the cold resonance as confirmed with the BPD (not depicted, see ref.[23]). The corresponding modeled $T_{rad,mod}$ values describe the measurements $T_{rad,ECE}$ reasonably well. This indicates that for the present case the equilibrium is not responsible for the displacement. In the chosen scenario the PRD is large compared to the uncertainty of the equilibrium. The equilibrium was validated using tomographic reconstruction of the soft X-ray measurements[28]. For this case the soft X-ray reconstruction allows one to determine
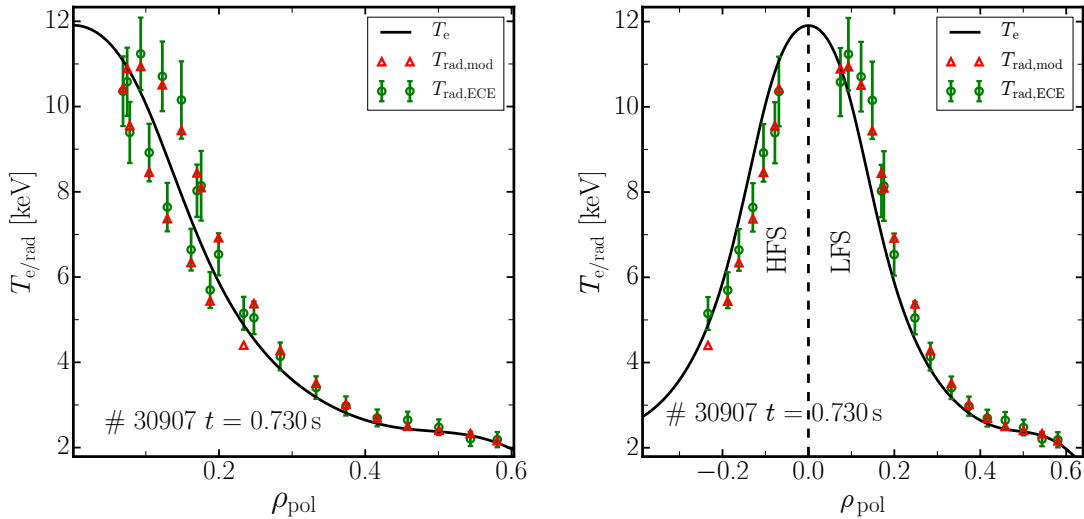
FIG. 6.   Loop structure of measured $T_{\rm rad,ECE}$ as a function of the magnetic coordinate and the $T_{\rm e}$-profile estimated using radiation transport modeling in the framework of IDA. In the right figure cold resonance positions on the HFS have negative normalized coordinates.

the magnetic axis with an upper uncertainty margin of 1 cm. Shifting the magnetic axis by 1 cm in any direction affects the HFS-LFS asymmetry of the ECE measurements negligibly. Radiation transport modeling intrinsically considers the PRD without the need for extra displacement of the emission location for subsequent estimation of the $T_{\rm e}$-profile as proposed by e.g. ref.[29]. This is very convenient for routine analysis of large data sets.

B.   3rd harmonic and harmonic overlap

The application of ECE for high $n_{\rm e}$ operation is limited by cut-offs, which is expected to hamper the use of the ECE diagnostic in future fusion devices. One solution to this problem is to measure the emission of a higher harmonic. In the case of ASDEX Uprade one can measure third harmonic X-mode instead of second harmonic, which increases the cut-off density by a factor of 1.5 compared to $X2$-mode. However, this approach is of limited applicability for two reasons. The first is that the absorption coefficient of the $X3$-mode resonance in medium size devices like ASDEX Upgrade is small. This broadens the BPD significantly compared to the BPD of second harmonic emission. The second challenge is given by the harmonic overlap. Typically, the cold resonance position of third harmonic

15

ECE lies on the LFS and it can be accompanied by an additional resonance with the second harmonic on the HFS. The combination of the low optical depth of the third harmonic resonance with the harmonic overlap can cause the second harmonic emission from the HFS to shine through the absorption layer of the third harmonic[30]. Hence, in order to estimate the T_e-profile the mixture of $X2$ and $X3$ emission needs to be modeled properly.
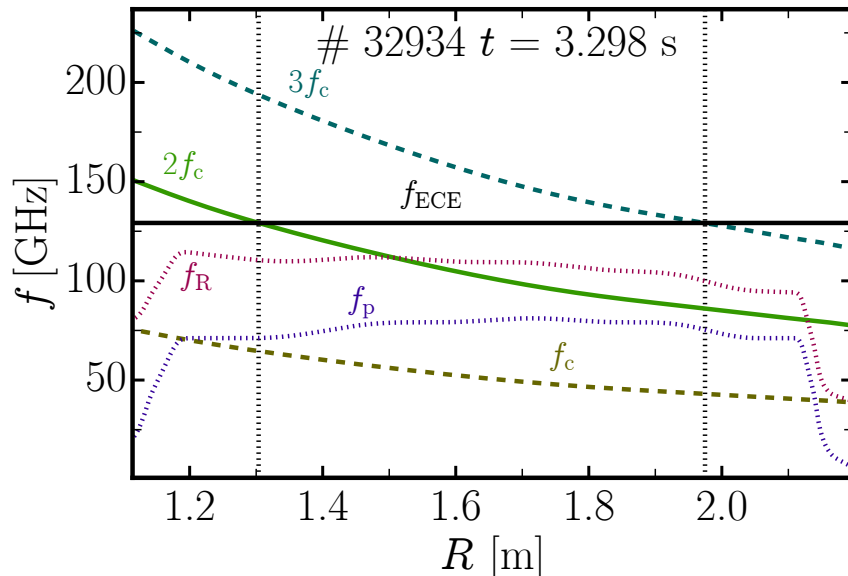

FIG. 7. # 32934 at $t = 3.298$ s: Radial dependence of the first, second and third harmonic of the cyclotron frequency f_c, the plasma frequency f_p, the right hand cut-off frequency f_R and a measurement frequency of 129 GHz.

An example of harmonic overlap is illustrated in figure 7 for the ASDEX Upgrade discharge #32934 at $t = 3.298$ s with magnetic field $B_t = -1.8$ T and a plasma core $n_e \approx 7.4 \times 10^{19}$ m^{-3}. Figure 7 shows the corresponding plasma frequency f_p, the right-hand cut-off frequency f_R, and the fundamental, second and third harmonic of the cyclotron frequency f_c. For a measurement frequency of $f_{ECE} < 105$ GHz the emission of the $X2$-mode is inaccessible for the entire LFS ($R > 1.65$ m), because the right-hand cut-off frequency $f_R > 2f_c$. In contrast, an increased measurement frequency of $f_{ECE} > 129$ GHz is not in cut-off, but introduces the problem of harmonic overlap.

At DIII-D the harmonic overlap has been addressed by calculating the optical depth of the $X3$ resonance and by evaluating T_{rad} from the mixture of $X2$ and $X3$ radiation under the assumption of $T_{rad} = T_e$ at the positions of both cold resonances[30]. Compared to

the rigorous treatment employing radiation transport modeling, the DIII-D approach has two disadvantages. The first is that the method inherently requires TS measurements to determine T_e at the cold resonance position of the second harmonic. The second disadvantage is that any relativistic broadening of either resonance is neglected.
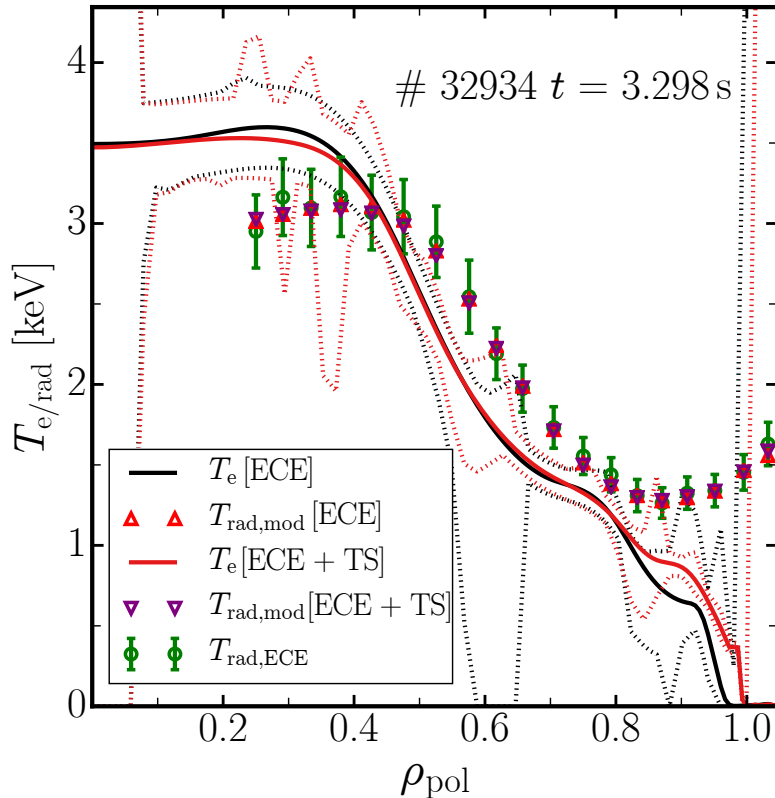

FIG. 8. T_e profiles and their corresponding uncertainties (dashed lines) estimated from ECE measurements ($T_{rad,ECE}$) only ($T_e[ECE]$) and from the combined analysis of ECE and TS data ($T_{e,TS}$) ($T_e[ECE+TS]$). The ECE measurements are mapped to the third harmonic cold resonance positions. Both sets of modeled ECE measurements $T_{rad,mod}[ECE]$ and $T_{rad,mod}[ECE+TS]$ agree reasonably well indicating the lack of information in the ECE data for $\rho_{pol} > 0.8$.

The radiation transport model in the IDA framework allows one to determine the T_e profile by only considering T_e information from ECE measurements. This works for any plasma region provided that significant local T_e information is supplied by the ECE measurements. Figure 8 shows #32934 at $t = 3.298\,\mathrm{s}$ where harmonic overlap has to be considered for nearly all channels. Please note that, in contrast to the previous figures, the measured $T_{rad,ECE}$ is

mapped to the cold resonance position of the third harmonic. The black line depicts the T_e-profile estimated from ECE measurements only. The red dashed lines indicate the upper and lower error band of the T_e-profile. Although for all measurement channels $T_{\mathrm{rad,ECE}}$ is matched very much, only the temperature in the region of $\rho_{\mathrm{pol}} < 0.8$ is reliable. The T_e-profile has large upper and lower uncertainty band for $\rho_{\mathrm{pol}} > 0.8$, because the ECE measurements do not provide any information on the T_e profile in this region. Figure 9 shows the BPDs for three selected channels. The black line corresponds to a channel with $X2$-resonance at $\rho_{\mathrm{pol}} = 0.88$ on the HFS and with $X3$-resonance at $\rho_{\mathrm{pol}} = 0.48$ on the LFS. Only the $X3$-mode contributes significantly to the measured intensity. The $X3$-mode emission is broad with a significant down-shifted contribution. The red line corresponds to a channel with $X2$-resonance at $\rho_{\mathrm{pol}} = 0.71$ on the HFS and with $X3$-resonance at $\rho_{\mathrm{pol}} = 0.90$ on the LFS. Both harmonics contribute to the measured intensity. The blue line corresponds to a channel with $X2$-resonance at $\rho_{\mathrm{pol}} = 0.66$ on the HFS and with $X3$-resonance in the SOL ($\rho_{\mathrm{pol}} = 1.01$). Although mapped in figure 8 to the third harmonic resonance position only $X2$-mode emission contributes to this channel. The combination of decreasing contribution from the $X3$-mode in the LFS region $\rho_{\mathrm{pol}} > 0.90$ and the small $X2$-mode emission on the HFS for $\rho_{\mathrm{pol}} > 0.90$ results in missing information about T_e in this region.

Although the method intrinsically works without additional diagnostics, improved results in regions with poor ECE coverage can be obtained if the ECE measurements are supplemented with TS data. The red line in figure 8 depicts the T_e profile of the combined analysis $T_e[\mathrm{ECE+TS}]$ and the red dashed line the corresponding upper and lower error margins. For $\rho_{\mathrm{pol}} < 0.8$ TS does not provide significant additional information. It only confirms the ECE measurements. For $\rho_{\mathrm{pol}} > 0.8$ the lack of information from ECE is compensated by TS. The modeled values $T_{\mathrm{rad,mod}}[\mathrm{ECE}]$ and $T_{\mathrm{rad,mod}}[\mathrm{ECE + TS}]$ agree very much indicating that the large error bars for $\rho_{\mathrm{pol}} > 0.8$ in the T_e profile considering ECE only is indeed resulting from missing information.

V. CONCLUSIONS

An improved radiation transport model for ECE data forward modeling is compared to a previous model used for standard plasma scenarios at ASDEX Upgrade. The improved performance of the new modeling was highlighted with two plasma scenarios. For routine
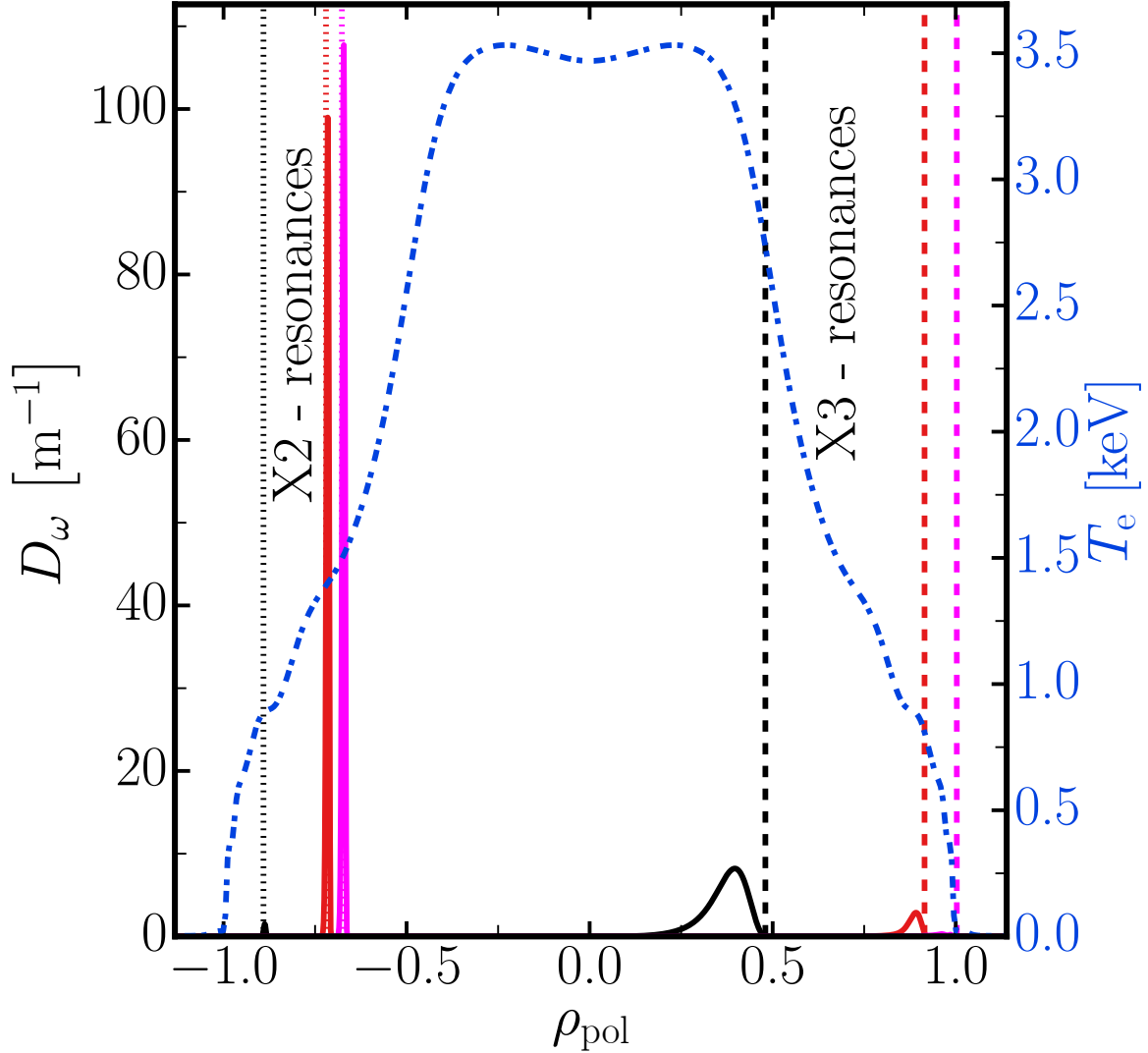
FIG. 9. T_e profile and BPDs for three channels shown in figure 8 at 3rd harmonic cold resonance ρ_{pol}-values of 0.48 (black), 0.90 (red) and 1.01 (magenta). The vertical lines show the 2nd (dotted) and 3rd harmonic cold resonance positions (dashed).

analysis of ECE data the improved modeling is indispensable.

The improved model includes cold plasma geometrical optics raytracing and a fully relativistic absorption coefficient considering cold plasma dispersion for the wave polarization and refractive index. The relativistic Maxwell-Jüttner distribution is the most important ingredient for describing properly the shine-through of heavily down-shifted emission from relativistic electrons in the plasma core. The effect of the radiation reaction force on the

high-energy tail of the electron distribution function and its consequence for the ECE measurement was investigated. The steady-state distribution arising from the radiation reaction function and relativistic collisions was calculated analytically and validated numerically. As a result, no significant effect on the modeled T_{rad} by the radiation reaction force can be found for the discussed scenarios. The residual discrepancy comparing measured and modeled T_{rad} is attributed to the simplified model for wall reflection.

The improved radiation transport model is applied to two plasma scenarios which constitute special cases from the perspective of ECE. The "pseudo-radial displacement" observed for large core T_{e}-gradients is automatically accounted for. The reconstruction of T_{e} profiles from ECE measurements containing a mixture of $X2$ and $X3$ emission is demonstrated. Supplementing the ECE data with TS data in the IDA framework helps to recover regions which are not covered properly by the ECE data alone.

The IDA approach including the advanced radiation transport forward model improves the accuracy of T_{e}-profile reconstructions and extends the operational space of the ECE diagnostic. The ECE forward model is applicable for routine analysis in everyday ECE data interpretation.

ACKNOWLEDGMENTS

Appendix A: Synchrotron radiation steady-state distribution

We want to find the steady-state distribution function of electrons taking the radiation reaction force into account. In the kinetic equation

$$C(f) = R(f) \tag{A1}$$

---

[1] http://www.euro-fusionscipub.org/eu-im

we have the collision operator[18],

$$C(f) = \frac{\gamma}{\tau u^3} \left[1 + Z - \varepsilon \frac{1 + 2u^2}{u^2 \gamma^2} \right] \mathcal{L}(f) + \frac{1}{\tau u^2} \frac{\partial}{\partial u} \left[\gamma^2 f + \varepsilon \frac{\gamma^3}{u} \frac{\partial f}{\partial u} \right], \tag{A2}$$

where $\mathcal{L}$ is the Lorentz scattering operator, $u = \gamma v/c$ the dimensionless momentum, $\zeta = u_\parallel/u$ the pitch-angle, $\gamma = (1 - v^2/c^2)^{-1/2}$ the Lorentz factor, $\tau = 4\pi\epsilon_0^2 m_e^2 c^3/(n_e e^4 \ln \Lambda)$ the collision time for relativistic electrons and $\varepsilon = T/m_e c^2$. The radiation reaction term is[17]

$$R(f) = \nabla_{\mathbf{u}} \cdot \left(f \left\langle \frac{\partial \mathbf{u}}{\partial t} \right\rangle_{\mathrm{rad}} \right) = \nabla_{\mathbf{u}} \cdot \left(f \frac{\partial \mathbf{u}}{\partial u} \left\langle \frac{\partial u}{\partial t} \right\rangle_{\mathrm{rad}} + f \frac{\partial \mathbf{u}}{\partial \zeta} \left\langle \frac{\partial \zeta}{\partial t} \right\rangle_{\mathrm{rad}} \right). \tag{A3}$$

In this expression, neglecting the radiation due to magnetic field curvature, we can express the radiation reaction force by

$$\left\langle \frac{\partial u}{\partial t} \right\rangle_{\mathrm{rad}} = -u\gamma \frac{1 - \zeta^2}{\tau_r} \tag{A4}$$

$$\left\langle \frac{\partial \zeta}{\partial t} \right\rangle_{\mathrm{rad}} = \zeta \frac{1 - \zeta^2}{\tau_r \gamma}, \tag{A5}$$

where $\tau_{\mathrm{r}} = 6\pi\epsilon_0 m_e^3 c^3/(e^4 B^2)$ is the radiation time scale. Note that in # 31539 $t = 2.814\,\mathrm{s}$, where $B = -2.5\,\mathrm{T}$, $n_e = 5.0 \times 10^{19}\,\mathrm{m}^{-3}$, $T_e = 9\,\mathrm{keV}$ and $\ln \Lambda \approx 17.5$, we have $\tau/\tau_{\mathrm{r}} \approx 0.05 \ll 1$. Thus, linearising $f(u, \zeta) = f_0 + f_1$, with $f_1 \ll f_0$, we find the solution to the lowest order equation $C(f_0) = 0$ to be the Maxwell-Jüttner distribution $f_0 = e^{-\gamma/\epsilon}$. To next order in τ/τ_{r} we have $C(f_1) = R(f_0)$, where

$$R(f_0) = \frac{1}{u^2} \frac{\partial}{\partial u} u^2 f_0 \left\langle \frac{\partial u}{\partial t} \right\rangle_{\mathrm{rad}} + \frac{1}{u^2} \frac{\partial}{\partial \zeta} u^2 f_0 \left\langle \frac{\partial \zeta}{\partial t} \right\rangle_{\mathrm{rad}} =$$
$$= -f_0 \frac{1}{\tau_{\mathrm{r}} u^2} \left[(1 - \zeta^2) \left(\frac{\partial}{\partial u} u^3 \gamma - \frac{u^4}{\varepsilon} \right) + \frac{(3\zeta^2 - 1)u^2}{\gamma} \right]. \tag{A6}$$

We express f_1 in Legendre polynomials $f_1 = f_0 \sum_{n=0}^{\infty} g_n(u) L_n(\zeta)$, and note that since $L_0 = 1$, $1 - \zeta^2 = 2(L_0 - L_2)/3$, $3\zeta^2 - 1 = 2L_2$ and $\mathcal{L}(L_n) = -n(n+1)L_n/2$ only the two components g_0 and g_2 are required. Using $\partial f_0/\partial u = -u/(\varepsilon\gamma)f_0$, we can write $C(f_1) = R(f_0)$ as

$$\varepsilon e^{\gamma/\varepsilon} \frac{d}{du} \left[e^{-\gamma/\varepsilon} \frac{\gamma^3}{u} \frac{dg_n}{du} \right] - \frac{\gamma}{u} \left[1 + Z - \varepsilon \frac{1 + 2u^2}{u^2 \gamma^2} \right] \frac{n(n+1)}{2} g_n =$$
$$= -\frac{\tau}{\tau_{\mathrm{r}}} \left[\frac{2}{3}(\delta_{n,0} - \delta_{n,2}) \left(\frac{d}{du} u^3 \gamma - \frac{u^4}{\varepsilon} \right) + \delta_{n,2} \frac{2u^2}{\gamma} \right], \tag{A7}$$

where $\delta_{i,j}$ is the Kronecker delta. We now proceed to solve this equation for $n = 0$ and $n = 2$.

21

For $n = 0$, Eq. (A7) becomes

$$\frac{d}{du}\left[e^{-\gamma/\varepsilon}\frac{\gamma^3}{u}\frac{dg_0}{du}\right] = -\alpha e^{-\gamma/\varepsilon}\left(\frac{d}{du}u^3\gamma - \frac{u^4}{\varepsilon}\right)$$

$$e^{-\gamma/\varepsilon}\frac{\gamma^3}{u}\frac{dg_0}{du} = -\alpha u^3\gamma e^{-\gamma/\varepsilon} + C, \tag{A8}$$

where we have defined $\alpha \equiv 2\tau/(3\tau_{\mathrm{r}}\varepsilon)$. For g_0 not to grow exponentially we have to demand that the integration constant $C = 0$, which yields

$$g_0 = -\alpha\left(\arctan(u) - u + \frac{u^3}{3}\right) = -\alpha\left(\frac{u^5}{5} - \frac{u^7}{7} + \dots\right). \tag{A9}$$

The expansion breaks down where $g_0 \sim 1$, e.g., $u \gtrsim (15\tau_{\mathrm{r}}\varepsilon/(2\tau))^{1/5}$. In # 31539 $t = 2.814\,\mathrm{s}$, $\varepsilon \approx 0.02$ and the expansion becomes invalid for $u \gtrsim 1.4$, but we are mainly interested in energies below $\sim 300\,\mathrm{keV}$ i.e., $u \lesssim 1.2$.

For $n = 2$, Eq. (A7) becomes

$$\varepsilon\gamma^2 g_2'' - \left(u\gamma + \varepsilon\frac{2u^2 - 1}{u}\right)g_2' - 3\left[1 + Z - \varepsilon\frac{1 + 2u^2}{u^2\gamma^2}\right]g_2 = \alpha\frac{u^5}{\gamma}\left(\varepsilon\frac{4}{\gamma} - 1\right). \tag{A10}$$

We can start by solving this equation in the range where $u \sim 1$, assuming that this implies that $g_2'' \sim g_2' \sim g_2$. Note also that $\alpha \sim 1$ in our ASDEX Upgrade case. To zeroth order in ϵ, we obtain

$$g_2' + \frac{\beta}{u\gamma}g_2 = \alpha\frac{u^4}{\gamma^2}, \tag{A11}$$

where we have defined $\beta \equiv 3(Z + 1)$. The solution is

$$g_2 = \alpha\left(\frac{\gamma + 1}{u}\right)^\beta\left[\int_0^u \frac{u^4}{\gamma^2}\left(\frac{u}{\gamma + 1}\right)^\beta du + D\right], \tag{A12}$$

where D is an integration constant. Since equation (A10) has a regular singularity at $u = 0$, we expect the derivatives g_2'' and g_2' to become large at low velocities. The expression (A12) has the non-relativistic limit

$$g_2 = \alpha\left(Du^{-\beta} + \frac{u^5}{\beta + 5}\right) \tag{A13}$$

and when $u^2 \sim \epsilon$ all three terms on the left hand side of Eq. (A10) become comparable. With the new variable $x \equiv u/\sqrt{\epsilon}$ we get

$$\frac{d^2 g_2}{dx^2} - \frac{x^2 + 1}{x}\frac{dg_2}{dx} + \frac{3 - \beta x^2}{x^2}g_2 = -\alpha x^5\varepsilon^{5/2}, \tag{A14}$$

22

the solution to which should be matched at large x to Eq. (A13). At large x Eq. (A14) becomes

$$-x\frac{dg_2}{dx} - \beta g_2 = -\alpha x^5 \varepsilon^{5/2}. \tag{A15}$$

There are two cases depending on the magnitude of g_2. Either the left hand side terms balance, giving $g_2 = Ax^{-\beta}$ (which matches the first term in (A13)), or all terms of Eq. (A15) must be kept. In the latter case, we get $g_2 = \alpha x^5 \varepsilon^{5/2}/(\beta+5)$, which matches the second term in (A13). One can continue to look at what the corresponding two solutions to Eq. (A14) are, but since we are mainly interested in $u \sim 1$, we will neglect the term involving D in (A12) and (A13). As an interesting example, we take $Z = 1$, i.e., $\beta = 6$. The expression (A12) becomes

$$g_2 = \alpha \left(\frac{\gamma+1}{u}\right)^6 \left[\frac{32}{u}(\gamma-1) + 17u + \frac{u^3}{3} - 3u\gamma - 29\operatorname{arcsinh}(u) - \arctan(u)\right] =$$
$$= \alpha(\gamma+1)^6 \left(\frac{u^5}{704} + \mathcal{O}(u^7)\right). \tag{A16}$$

Figure 10 gives an idea of the upper limit for the validity of the assumption $f_1 \ll f_0$.
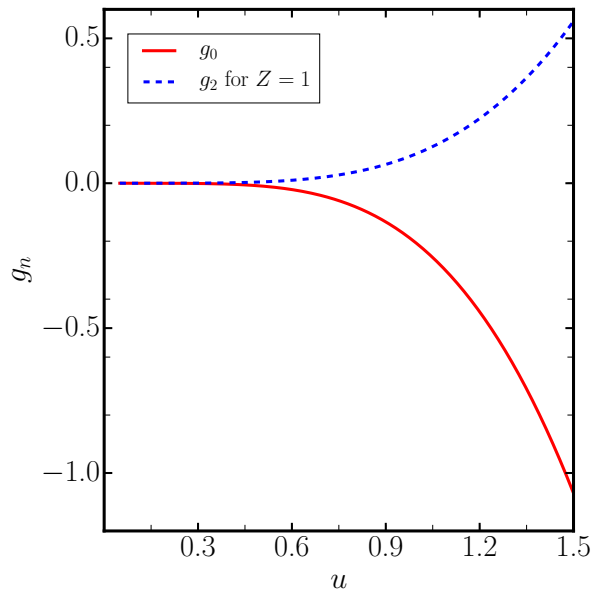

FIG. 10. g_0 and g_2 for the case $Z = 1$, $\alpha = 1.76$.

REFERENCES

[1] N. C. Luhmann, H. Bindslev, H. Park, J. Sánchez, G. Taylor, and C. X. Yu, Fusion Science and Technology **53**, 335 (2008), http://dx.doi.org/10.13182/FST08-A1675, URL `http://dx.doi.org/10.13182/FST08-A1675`.

[2] I. Hutchinson, *Principles of Plasma Diagnostics* (Cambridge University Press, 1987), ISBN 9780521326223, URL `https://books.google.de/books?id=iSy-QgAACAAJ`.

[3] E. d. l. Luna, J. Sánchez, V. Tribaldos, J.-E. contributors, G. Conway, W. Suttrop, J. Fessey, R. Prentice, C. Gowers, and J. M. Chareau, Review of Scientific Instruments **75**, 3831 (2004), URL `http://scitation.aip.org/content/aip/journal/rsi/75/10/10.1063/1.1781376`.

[4] S. K. Rathgeber, L. Barrera, T. Eich, R. Fischer, B. Nold, W. Suttrop, M. Willensdorfer, E. Wolfrum, and the ASDEX Upgrade Team, Plasma Physics and Controlled Fusion **55**, 025004 (2013), URL `http://stacks.iop.org/0741-3335/55/i=2/a=025004`.

[5] M. Sato, N. Isei, S. Ishida, and A. Isayama, Journal of the Physical Society of Japan **67**, 3090 (1998), http://dx.doi.org/10.1143/JPSJ.67.3090, URL `http://dx.doi.org/10.1143/JPSJ.67.3090`.

[6] I. G. J. Classen, C. W. Domier, N. C. Luhmann, A. V. Bogomolov, W. Suttrop, J. E. Boom, B. J. Tobias, A. J. H. Donné, and A. U. Team, Review of Scientific Instruments **85**, (2014).

[7] R. Fischer, C. J. Fuchs, B. Kurzan, W. Suttrop, E. Wolfrum, and the ASDEX Upgrade Team, Fusion Science and Technology **58**, 675 (2010), ISSN 1536-1055.

[8] S. S. Denk et al., in *19th Joint workshop (EC-19) on Electron Cyclotron Emission (ECE) and Electron cyclotron Resonance Heating (ECRH)* (EPJ, 2016).

[9] N. Salmon, International Journal of Infrared and Millimeter Waves **15**, 53 (1994), ISSN 0195-9271.

[10] H. J. Hartfuss, T. Geist, and M. Hirsch, Plasma Physics and Controlled Fusion **39**, 1693 (1997), URL `http://stacks.iop.org/0741-3335/39/i=11/a=001`.

[11] F. Albajar, N. Bertelli, M. Bornatici, and F. Engelmann, Plasma Physics and Controlled Fusion **49**, 15 (2007), ISSN 0741-3335.

[12] A. Mlynek, C. Angioni, E. Fable, R. Fischer, F. Ryter, J. Stober, W. Suttrop, H. Zohm, and the ASDEX Upgrade Team, Nuclear Fusion **52**, 114012 (2012), URL `http://stacks.`

iop.org/0029-5515/52/i=11/a=114012.

[13] M. Willensdorfer, E. Wolfrum, R. Fischer, J. Schweinzer, M. Sertoli, B. Sieglin, G. Veres, F. Aumayr, and the ASDEX Upgrade Team, Review of Scientific Instruments **83**, 023501 (2012).

[14] B. Kurzan and H. D. Murmann, Review of Scientific Instruments **82**, 103501 (2011), http://dx.doi.org/10.1063/1.3643771, URL `http://dx.doi.org/10.1063/1.3643771`.

[15] M. Willensdorfer, S. S. Denk, E. Strumberger, W. Suttrop, B. Vanovac, D. Brida, M. Cavedon, I. Classen, M. Dunne, S. Fietz, et al., Plasma Physics and Controlled Fusion **58**, 114004 (2016), URL `http://stacks.iop.org/0741-3335/58/i=11/a=114004`.

[16] F. Andersson, P. Helander, and L.-G. Eriksson, Physics of Plasmas **8**, 5221 (2001).

[17] E. Hirvijoki, J. Decker, A. Brizard, and O. Embréus, Journal of Plasma Physics **81** (2015).

[18] P. Sandquist, S. Sharapov, P. Helander, and M. Lisak, Physics of plasmas **13**, 072108 (2006).

[19] E. Westerhof, A. Peeters, and W. Schippers, *RELAX: A Computer Code for the Study of Collisional and Wave Driven Relaxation of the Electron Distribution Function in Toroidal Geometry*, Rijnhuizen report (FOM-Instituut voor Plasmafysica "Rijnhuizen", 1992), URL `https://aip.scitation.org/doi/suppl/10.1063/1.2727479/suppl_file/rr92-211.pdf`.

[20] W. H. M. Clark, Plasma Physics **25**, 1501 (1983), URL `http://stacks.iop.org/0032-1028/25/i=12/a=315`.

[21] G. Sichardt, E. Holzhauer, A. Köhn, M. Ramisch, and T. Hirth, in *44th EPS Conference on Plasma Physics* (2017).

[22] W. Suttrop and A. Peeters, *Practical Limitations to Plasma Edge Electron Temperature Measurements by Radiometry of Electron Cyclotron Emission*, Bericht / 1: Bericht (Max-Planck-Inst. für Plasmaphysik, 1996), URL `http://edoc.mpg.de/559557`.

[23] S. S. Denk, R. Fischer, O. Maj, E. Poli, M. Willensdorfer, J. Stober, U. Stroth, W. Suttrop, et al., in *44th EPS Conference on Plasma Physics* (2017), proceedings of the 44th EPS Conference on Plasma Physics.

[24] D. Bartlett, C. Bishop, R. Cahill, A. McLachlan, L. Porte, and A. Rookes, Tech. Rep., JET Joint Undertaking (1995).

[25] G. Garstka, M. Austin, and R. Ellis, Fusion Engineering and Design **53**, 123 (2001), ISSN 0920-3796, URL `http://www.sciencedirect.com/science/article/pii/`

S0920379600004865.

[26] J. L. Ségui, D. Molina, and M. Goniche, in *Electron Cyclotron Emission and Electron Cyclotron Heating*, edited by G. Giruzzi (2003), pp. 209–214.

[27] R. Fischer, J. Hobirk, L. Barrera, A. Bock, A. Burckhart, I. Classen, M. Dunne, J. Fuchs, L. Giannone, K. Lackner, et al., in *40th EPS Conference on Plasma Physics* (2013), proceedings of the 40th EPS Conference on Plasma Physics.

[28] T. Odstrčil, T. Pütterich, M. Odstrčil, A. Gude, V. Igochine, and U. Stroth, Review of Scientific Instruments **87**, 123505 (2016).

[29] J. Ségui, D. Molina, G. Giruzzi, M. Goniche, G. Huysmans, P. Maget, M. Ottaviani, and T. S. Team, Review of scientific instruments **76**, 123501 (2005).

[30] M. E. Austin, R. F. Ellis, R. A. James, and T. C. Luce, Physics of Plasmas **3**, 3725 (1996), http://dx.doi.org/10.1063/1.871506, URL http://dx.doi.org/10.1063/1.871506.